AIAA JOURNAL
Vol. 44, No. 3, March 2006

Boundary Condition Effects on Nonreacting and Reacting Flows in a Multiswirl Combustor

Guoqiang Li* and Ephraim J. Gutmark†
University of Cincinnati, Cincinnati, Ohio 45220

Detailed measurements of velocity statistics, temperature distribution, flame chemiluminescence, and emission characteristics in a lean direct fuel injection multiswirl gas turbine combustor are presented. The inlet and exit boundary conditions, including the mixing tube length and the exhaust nozzle contraction ratio, were modified to emphasize the effects of these boundary conditions on the characteristics of nonreacting and reacting flows. Velocity statistics, including mean and turbulence kinetics, were measured by using stereoscopic particle image velocimetry in a cylindrical combustor chamber for isothermal and reacting flow cases. The velocity spectra at different locations were measured using hot-wire anemometry. The temperature distribution along the combustor radial direction was measured using type-B fine thermocouple at different axial locations for a variety of multi-swirl configurations. The exhaust emissions of NO_x and CO were measured as a function of fuel/air ratio. The data along with the detailed description of the experimental setup and operating conditions can be used to validate modeling approaches to swirling flows, the turbulence/chemistry interaction, and large-eddy simulation for multiswirl gas turbine combustors.

Nomenclature

C_R	=	contraction ratio of exhaust nozzle
D	=	diameter of swirler exit
D_c	=	diameter of combustion chamber
f	=	frequency
k	=	turbulence kinetic energy
L_{mt}	=	nondimensional length of mixing tube
m_a	=	mass flow rate of air
p_3	=	plenum pressure
R	=	radius of swirler exit
r	=	radial coordinates
Sr	=	Strouhal number
T_3	=	air inlet temperature
T_4	=	combustion gas temperature
V_r	=	radial velocity component
V_z	=	axial velocity component
V_θ	=	tangential velocity component
V_0	=	averaged axial velocity based on swirler exit
z	=	axial coordinates
Φ	=	fuel equivalence ratio
Φ_{LBO}	=	fuel equivalence ratio at lean flame blowoff

I. Introduction

INCREASINGLY stringent regulations of pollutant emissions of gas turbine engines, particularly regarding low emissions of oxides of nitrogen (NO_x), require development of new concepts of combustion systems.[1] A typical method of reducing NO_x formation is by operating the combustor in a lean premixed combustion mode near the lean blowout limit (LBO). This type of approach results in efficient combustion with extremely low emissions and improved combustor performance. Lean premixed combustors achieve NO_x emission levels below 10 ppm at atmospheric pressure and below 25 ppm at gas turbine operating conditions.[2,3] The reliability of lean premixed combustion systems is problematic because they operate close to the lean stability limit and are more susceptible to combustion instabilities, flame blowout, and flashback.[4]

As an alternative approach, lean direct fuel injection (LDI) combustion, one of the new concepts that is applied in nonpremixed combustion, is developed to reduce NO_x emissions through the arrangement of multiple counter-rotating or corotating air swirlers with a distributed fuel injection system.[5,6] Such an arrangement allows control of the mixing pattern, flame structure, and temperature via airflow control and fuel distribution to prevent drawbacks associated with premixing flames, such as autoignition and flashback.[7,8] Experimental study[8] showed that the NO_x emissions for a LDI-type double-swirler burner were less than half of the conventional small-hub and large-hub swirlers. LDI combustors are advantageous in providing low NO_x emissions with lower susceptibility to combustion dynamics and, thus, provide an attractive alternative for application in aircraft gas turbine engines. The triple annular research swirler, which has been developed through collaboration with General Electric Aircraft Engines and Goodrich Aerospace, features the generic design of LDI fuel injectors with three individual air swirlers coupled with two separate fuel supply lines for liquid fuel. This nozzle/swirler assembly can also be configured for use with gaseous fuels.

Large eddy simulation (LES), which is a computational fluid dynamics (CFD) technique bridging direct numerical simulation and Reynolds-averaged Navier–Stokes (RANS) simulation, provides cost-effective solution for simulating complex unsteady flows by filtering the flow, solving the large eddies that are dominant terms of the turbulence spectra and handling the smallest eddies by subgrid-scale (SGS) models. This approach has been extensively studied and applied in swirling flows of gas turbine combustors to simulate dynamic swirling flow structures for isothermal flow[9,10] and predicting the emissions[11] in combustion cases. In all such applications, the validation of LES codes is crucial. Good-quality experimental data with well-defined boundary conditions are highly desirable for the computational community. However, few experimental data are available for multiple swirl flows, especially data covering velocity statistics, temperature distribution, emissions, and combustion dynamics. This study intends to provide laboratory data on a LDI multiswirl low-emissions combustor, the triple annular research swirler (TARS), with different inlet and outlet boundary conditions. To avoid complicated issues associated with

Received 21 January 2005; revision received 28 April 2005; accepted for publication 10 August 2005.

*Research Assistant Professor, Department of Aerospace Engineering and Engineering Mechanics. Member AIAA.
†Ohio Eminent Scholar, Department of Aerospace Engineering and Engineering Mechanics. Associate Fellow AIAA.

spray combustion, data presented in this paper are limited to gaseous fuel combustion, although tests on spray combustion have also been conducted.

II. Experimental Setup

The core of the low NO_x LDI combustor is the TARS, which was developed by Delavan Gas Turbine Products, a division of Goodrich Corporation, in collaboration with General Electric Aircraft Engines. (Two- and three-dimensional drawings of TARS and the combustor geometry are available at http:\\www.ase.uc.edu\~fluidlab\project\TARS\Drawings, 2005.) TARS (Fig. 1) features three air passages, each with an individual swirler. Different configurations of TARS can be realized by changing the swirlers, outer swirler α, intermediate swirler β, and inner swirler γ, to either different swirling vane angles or different rotating directions, to form different swirling flowfields. The inner and intermediate swirlers are axial swirlers, whereas the outer swirler is radial. Hereafter, the swirler configuration will be labeled with the swirler angle in the order of outer, intermediate, and inner, and with C labeling the counter-rotating swirl direction. For example, S5545C45 denotes that this mixer's outer, intermediate, and inner swirlers' vane angles are 55, 45, and 45 deg, respectively. The outer and inner swirler corotate, whereas the intermediate swirler counterrotates. The overall length of TARS is 66 mm (2.6 in.) and the diameter of the outer swirler exit is 50.8 mm (2 in.). The intermediate swirler is located 66 mm (2.6 in.) upstream of TARS exit, whereas the inner swirler is at 50.8 mm (2 in.) upstream of TARS exit plane.

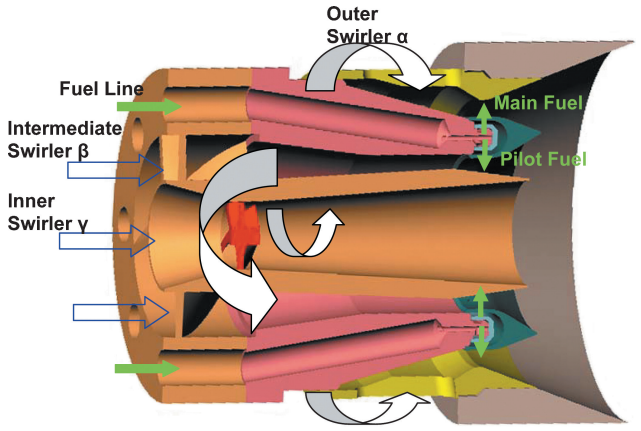

Fig. 1 Section view of TARS.

Two sets of distributed fuel injection circuits are integrated within the TARS assembly: The pilot fuel circuit injects fuel inward into the intermediate swirling air passage, and the main fuel circuit injects fuel outward into the outer swirling air passage. Gaseous fuel is injected through both the pilot and main fuel circuits. The number of injection holes for the pilot and main fuel is four and eight, respectively. All of the injection holes are identical, 0.762 mm (0.03 in.) in diameter. These injection holes are perpendicular to the wall so that the gaseous fuel is injected normal to the airstreams.

The atmospheric combustion test rig with the TARS fuel injector is shown in Fig. 2. The rig consists of an inlet flange, flow conditioning chamber (609.6 mm, 24 in. long), plenum chamber (361.9 mm, 14.25 in. long), and the combustion chamber. The flow conditioning and plenum chambers are constructed of 6-in. schedule 80 stainless-steel pipes with inner diameter of 133.4 mm (5.25 in.). When it is flowing through the flow conditioning chamber, the flow passes through a perforated cone and then through a sequence of five fine-mesh screens whose mesh size is gradually reduced to 0.05-mm

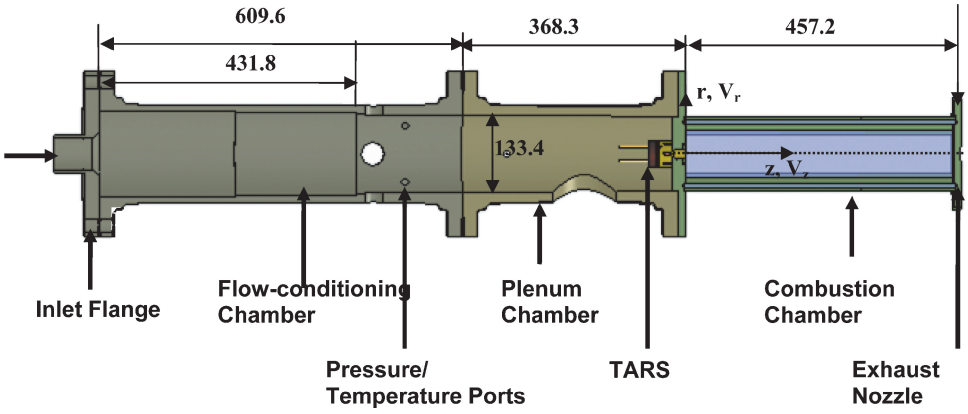

a) Test rig

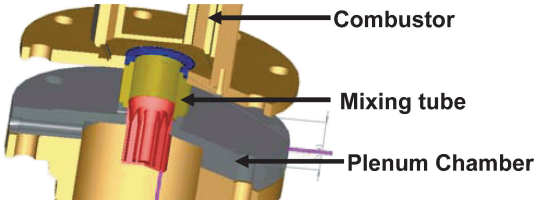

b) Three-dimensional mixing tube

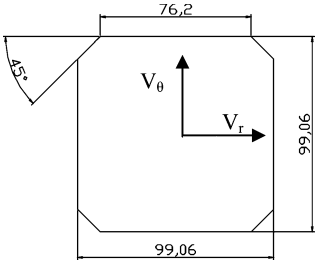

c) Cross-sectional view of octagonal combuster

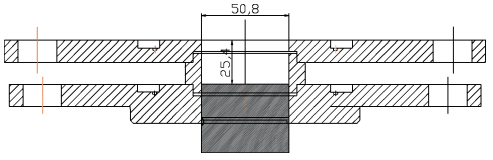

d) Streamwise-section view of mixing tube $L_{mt} = 0.5$

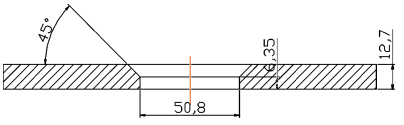

e) Section view of exhaust nozzle, $C_R = 4$

Fig. 2 Detailed drawings of the various test rig sections.

Table 1 Geometrical parameters of the atmospheric combustion test rig

Parameter	Value
Combustor diameter (cylindrical type)	101.6 mm (4 in.), D_C
Combustor inlet diameter	50.8 mm (2 in.), $0.5D_C$
Inner diameter of fuel injection hole	0.762 mm (0.03 in.)
Length of cylindrical combustor	457.2 mm (18 in.), $4.5D_C$
Length of octagonal combustor	457.2 mm (18 in.), $4.5D_C$
Intermediate swirler location from the combustor inlet plane	66 mm (2.6 in.), $0.65D_C$
Inner swirler location from the combustor inlet plane	50.8 mm (2 in.), $0.5D_C$
Outer swirler cone diameter	50.8 mm (2 in.), $0.5D_C$
Length from the final stage screen to the combustor inlet	546.1 mm (21.5 in.)

(0.002-in.) diameter with 44% open area ratio. The fuel injector, TARS, is centered on a mounting plate (6.35 mm, 0.25 in. thick) and flush mounted with the combustor chamber inlet.

Two types of combustion chambers were utilized in this study. The first one is a 457-mm (18-in.)-long cylindrical quartz tube, with a 101.6 mm (4 in.) inner diameter, and a 2.5-mm wall thickness. Data on the velocity statistics, flame images, and emissions were taken from tests performed with this cylindrical combustor. The second combustion chamber had an octagonal cross-sectional shape with three 5-mm-thick flat quartz walls and one stainless steel wall that was instrumented with thermocouples. The cross-sectional area of the octagonal combustor, whose dimensions are shown in Fig. 2c, is identical to the cylindrical one. Temperature measurements were performed in the octagonal combustor because it provided optical access for flame imaging while avoiding the difficulty of drilling thermocouple access holes on the cylindrical quartz tube. A short mixing tube (Fig. 2b) can be inserted between the TARS exit and the combustor dump plane. This mixing tube has the same inner diameter as the TARS exit. The total length of the mixing section, L, composed of the mixing tube, sealing gasket, and the mounting plate, is normalized by the diameter of the TARS exit, D, as $L_{\mathrm{mt}} = L/D$. Figure 2d is the streamwise-sectional view of the mixing section with $L_{\mathrm{mt}} = 0.5$. The combustion products exit the combustor through a circular exhaust nozzle (Fig. 2e). The contraction ratio is defined as the ratio between the exhaust nozzle and the combustion chamber areas, C_R. The geometrical parameters of the experimental setup are summarized in Table 1. A 90 by 45 cm rectangular exhaust hood is installed 80 cm above the combustor exhaust nozzle. The exhaust hood is bent into horizontal direction and then connected to an exhaust fan at about 5 m downstream.

The rig is set up vertically with the combustion air preheated by a 36-kW electric heater to the desired temperature flowing through the inlet flange into a flow conditioning chamber. A static pressure transducer (Druck PMP 4000 series, $\pm 0.04\%$ full scale (FS) accuracy, 6894.8-Pa range) and a type-K thermocouple were mounted in this chamber to monitor the pressure drop, dynamics pressure oscillations, and inlet air temperature. The air mass flow rate was metered by a digital flow meter (Eldridge Prouducts, Inc., 1% accuracy). The gaseous fuel flow was set at 206,843 Pa controlled by a needle valve and metered by a digital gas flow meter (Alicat M series, $\pm 1\%$ FS accuracy).

The gas sampling and analysis system was an extractive sample conditioning and control system, which provided a representative sample to a chemiluminescence NO_x monitor and an infrared CO monitor with an installed paramagnetic O_2 sensor. The system has a 10 parts per billion (ppb) resolution for NO/NO_x, 0.1 ppm for CO, with 0.1% for CO_2 and O_2. The sampling line was heated to above 100°C to avoid water vapor condensation. The CO analyzer is designed to be in a serial arrangement using a pneumatic-type differential sensor to minimize the interference from CO_2 or water vapor. All process parameters, including main airflow rate m_a, air inlet temperature T_3, plenum pressure p_3, pressure inside combustion chamber p_4, combustion gas temperature T_4, combustor wall temperature T_w, total fuel flow rate W_f, and the emissions data from the gas analyzer were recorded by Labview software.

A stereoscopic particle-image velocimetry (PIV) system was used to measure the velocity flowfield inside the combustion chamber. The system included two 120-mJ, 15-Hz pulsed Nd-Yag lasers (New Wave Research Gemini PIV laser Model 120-15), TSI PIV signal synchronizer, two 2048×2048 pixel 12-bit Powerview charge-coupled device (CCD) cameras, and two high-performance frame grabbers. The 4-mm-diam laser beam from the laser head was spread by a cylindrical lens (with focal length equal to -15 or -25 mm or combination of two) and a spherical lens (with focal length equal to 500 mm) into a laser sheet. The laser sheet was about 130 mm wide and 1 mm thick at the location of the beam waist, which overlapped the centerline of the combustion chamber.

For measurements in the streamwise plane (including the combustion chamber axis), the two CCD cameras were at the same side of the laser sheet with a separation angle of 30 deg, focusing on the field of view created by the pulsed laser sheet in the streamwise plane (r–z plane in Fig. 2a). Based on the displacement of pixels between the two laser pulses (where, in this experiment, the laser pulse interval was between 6 and 12 μs), the radial velocity V_r and axial velocity V_z were obtained with units of pixels per second. To obtain the tangential velocity component V_θ, which was perpendicular to the laser sheet, a calibration procedure was applied to generate the correlation equation by imaging several (normally two) planes with different depth in the perpendicular direction.

A type-B thermocouple (6%Rh/Pt–30%Rh, 10-mil lead wire) with ceramic insulation tube was mounted on a two-dimensional traverse system to map the temperature field. All temperature data were corrected for radiation effects by using the equation[12]

$$T_g = T_{tc} + \varepsilon_{tc}\sigma\left(T_{tc}^4 - T_w^4\right)d\big/kNu \tag{1}$$

where the emissivity $\varepsilon_{tc} = 0.22$, the Stefan–Boltzmann constant $\sigma = 5.67 \times 10^{-8}$ J K^{-4} m^{-2} s^{-1}, and the bead diameter $d = 0.03$ in. $= 0.762$ mm. Thermal conductivity for air at 1450 K $k = 0.0924$ W/m · K, and the Nusselt number $Nu = 5.05$ based on the bead diameter and evaluated at 1500 K air according to the correlation[12]

$$Nu_{d,\mathrm{sph}} = 2.0 + 0.6Re_d^{\frac{1}{2}}Pr^{\frac{1}{3}} \tag{2}$$

All flow meters in this study have accuracy of $\pm 1\%$. The fuel/air equivalence ratio is defined as the actual fuel/air ratio divided by the stoichiometric ratio. The error in the fuel and airflow rates contributed $\pm 1.4\%$ using the root mean square method. The Reynolds number was calculated from the air mass flow rate at the fuel nozzle exit, fluids properties (density and viscosity), and geometry. Because the errors in fluid properties and geometry were small, the error in Reynolds number is estimated to be 1%. Inlet air temperature was measured by type-K thermocouples with ± 1°C accuracy. The combustion temperature was measured with a type-B thermocouple and precision thermometer with accuracy ± 0.1°C.

It is difficult to describe accurately the measurement error associated with PIV. The comparison of velocity profiles in similar TARS flowfield measured by PIV and laser Doppler velocimetry (LDV) reveals that the PIV measurement has about 5∼10% error because LDV measurement is based on average of thousands of data points and is believed to be more accurate. Regarding the accuracy of the measurement location, although the PIV system is carefully aligned so that the centerline of the combustor is at the center mark of the calibration target, which is also the zero coordinate of the measurement, it does not ensure that this centerline is exactly overlapping the geometrical centerline because the target plate is placed inside the circular quartz, which causes distortion. This position error is estimated to be 2.5 mm (0.1 in.) based on comparison between the measured flowfield centerline and the zero coordinate.

III. Results and Discussion

Vortex breakdown in ducted swirling flows, such as in the present combustion chamber, causes the formation of a central recirculation

zone (CRZ), with reversed flow near the axis. This CRZ is either of spherical or spiral shape, depending on the swirl strength and inlet flow Reynolds number. Swirling flows are three dimensionally unsteady, and their dynamics are sensitive to geometrical factors. In the present study, the velocity statistics, velocity spectra, temperature distribution, OH* chemiluminescence images, and emissions characteristics are first presented for the baseline case (defined later). Following that, the effects of the inlet mixing tube length L_{mt} and the contraction of the combustor exhaust nozzle, C_R, on the swirling flowfield, temperature distribution, and emissions are presented and discussed. The coordinates were normalized by the TARS exit radius $R = 25.4$ mm.

A. Baseline Case

The baseline is a coswirling case, with swirler geometry of S554545, in which all three swirlers are in the clockwise direction when observed from the upstream direction. There is no mixing tube ($L_{\mathrm{mt}} = 0$), and no exhaust nozzle contraction ($C_R = 1$), that is, the combustion chamber is not constricted at the exit.

1. *Velocity Field*

The nonreacting cold flowfield is characterized first, followed by a gradual increase of the inlet air temperature to study the effect of temperature, and finally the velocity statistics for stable and unstable combustion are evaluated.

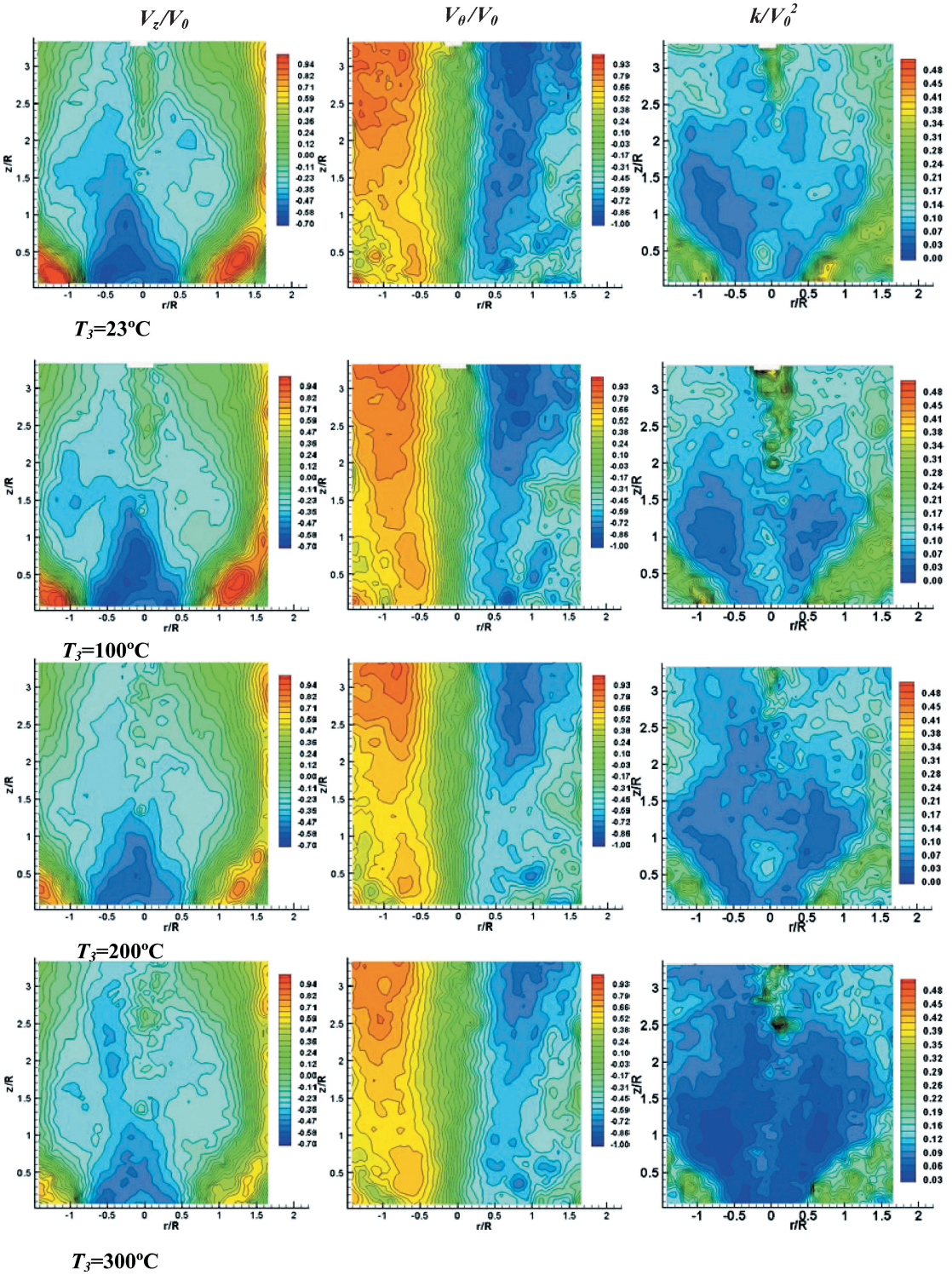

Fig. 3 Contours of V_z/V_0, V_θ/V_0, and k/V_0^2 at $T_3 = 23$, 100, 200, and 300°C: $m_a = 0.032$ kg/s, $L_{\mathrm{mt}} = 0$, and $C_R = 1$.

Table 2 Test conditions for nonreacting and reacting flows

Case description	Mass flow rate W_a, g/s	Pressure drop Δp, psi	Inlet temperature T_3, °C
Cold flow case	32	0.425	23
Isothermal flow case 1	32	0.548	100
Isothermal flow case 2	32	0.623	200
Isothermal flow case 3	32	0.785	300
Isothermal flow case 4	32	0.76	230
Combustion flow (stable)	32	0.80	230
Combustion flow (unstable)	32	1.05	230

Velocity field of nonreacting swirling flows. The mass flow rate, the pressure drop across the swirler, and the inlet air temperature for the tests of nonreacting flow and reacting flow are listed in Table 2. The mass flow rate was kept constant for the cold, isothermal, and reacting flow cases. Inlet air temperature T_3 is a major factor for gas turbine combustion performance; therefore, knowledge of its effects on the swirling flowfield is necessary for combustor design and combustion performance improvement. For the same air mass flow rate, high temperature increases the bulk velocity and viscosity, significantly changing the inlet Reynolds number and potentially affecting the swirling flow dynamics.

Figure 3 shows the contours of normalized axial, tangential, and total turbulence velocity inside the circular combustion chamber for $T_3 = 23$–$300°$C. Axes r and z are in the radial and axial directions, respectively, as shown in Fig. 2a. V_r, V_z, and V_θ are the radial, axial, and tangential velocity components, respectively. Because V_θ is the out-of-plane circumferential component, its direction is opposite on the two sides of the centerline as shown with contrasting colors in the contour plot. The total turbulent kinetic energy (TKE) k is defined as the sum of the squares of the three velocity components' fluctuations as $k = \frac{1}{2}\left(\bar{V}_r'^2 + \bar{V}_z'^2 + \bar{V}_\theta'^2\right)$. Because the mass flow rates were kept constant, $m_a = 0.032$ kg/s, the average TARS exit velocity V_0 was calculated from the volumetric flow rate as 13, 16, 21, and 25 m/s for $T_3 = 23$, 100, 200, and 300°C, respectively. The velocity components V_z and V_θ and the TKE k were normalized with V_0 as V_z/V_0, V_θ/V_0, and k/V_0^2. From the contours of V_z/V_0, it can be seen that the CRZ has approximately a spherical shape for all of the velocity fields in the temperature range $T_3 = 23$–$300°$C, as indicated by the blue color in Fig. 3. The width of the CRZ is $\pm 0.6R$ at the exit of TARS ($z/R = 0.1$) and increases to $\pm 1.3R$ at $z/R = 1.5$. Farther downstream, the CRZ's size reduces. Outside the CRZ is the region of an annular jet that emanates from the swirler, as represented by the red and orange colors. In the present paper, this region is noted as the swirling jet in contrast to the CRZ region. The specific characteristics of the mean velocity field were also shown in the contours of V_θ/V_0 with low V_θ near the centerline at $r/R = 0$ and a high V_θ region near $z/R = 3$, $r/R = 1$. The contours of k/V_0^2 show the distribution of the total turbulence: The turbulence is strongest at the shear layer between the swirling jet and the CRZ and is lower inside the CRZ. The turbulence intensity in the shear layer is more than twice the level in the CRZ.

To quantify the observations from these contours, the profiles of V_z/V_0, V_θ/V_0, and k/V_0^2 at $z/R = 0.5$ of Fig. 3 are compared in Fig. 4. The similarity of mean velocity distribution inside the CRZ is obvious in the profiles of V_z/V_0 and V_θ/V_0. For $T_3 = 23$–$300°$C, the zero V_z/V_0 is located at $\pm 1R$ (Fig. 4a) and the vortex core (solid body rotation region) is between $\pm 0.5R$ (Fig. 4b). Also note that the profiles are scattered in the swirling jet region (beyond $\pm 1R$ in both Figs. 4a and 4b). Inlet temperature affected the turbulent velocity k/V_0^2, particularly in the core ($\pm 0.5R$) and in the jet region (beyond $\pm 1R$). In summary, the mean velocity field preserved its characteristics with the increase of T_3, but the magnitude of the velocity components was significantly different because the bulk velocity increases whereas the mass flow rates were kept constant.

Velocity field of the reacting swirling flows. The velocity field of the reacting swirling flow differs from the isothermal one as a result of the changes in the temperature and the density due to the combustion heat release. The operating parameters of mass flow rate, pressure drop, and inlet temperature of the present measurements

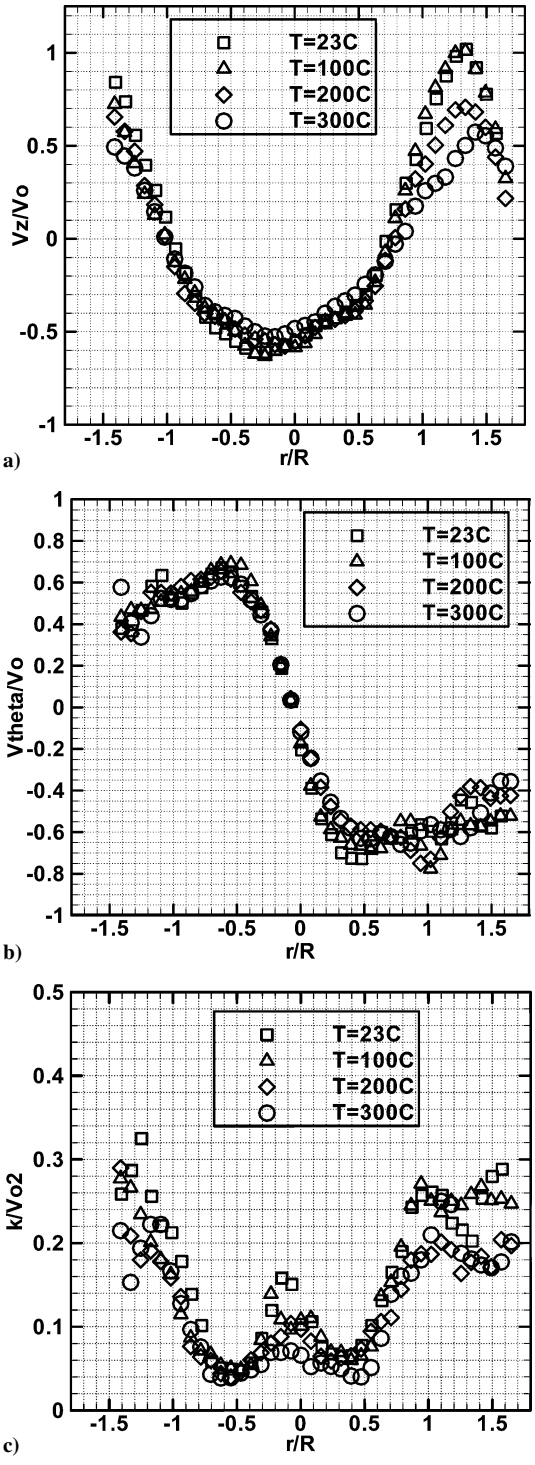

Fig. 4 Profiles at $z/R = 0.5$ for $T_3 = 23 \sim 300°$C, $m_a = 0.032$ kg/s, $L_{mt} = 0$, and $C_R = 1$: a) V_z/V_0, b) V_θ/V_0, and c) k/V_0^2.

are listed in Table 2. Note that, at the same inlet temperature and mass flow rates, the pressure drop is considerably higher for unstable combustion compared to the stable case. A comparison of V_z/V_0 and k/V_0^2 for isothermal, stable, and unstable combustion flows is shown in Fig. 5. The airflow rate is kept 0.032 kg/s for all cases, and V_0 is 23 m/s at $T_3 = 230°$C. The jet-A fuel flow rates for the stable and unstable combustion cases are 1.89 and 3.22 g/s, corresponding to equivalence ratios 0.5 and 0.85, respectively. The CRZs for all three cases had a spherical shape but were quite different in size and location relative to the swirler exit. For stable combustion, the CRZ is lifted and the constriction near the swirler exit ($z/R = 0$) becomes significantly smaller, only $\pm 0.2R$ compared to $\pm 0.7R$ for the isothermal case. When unstable combustion occurred, the CRZ

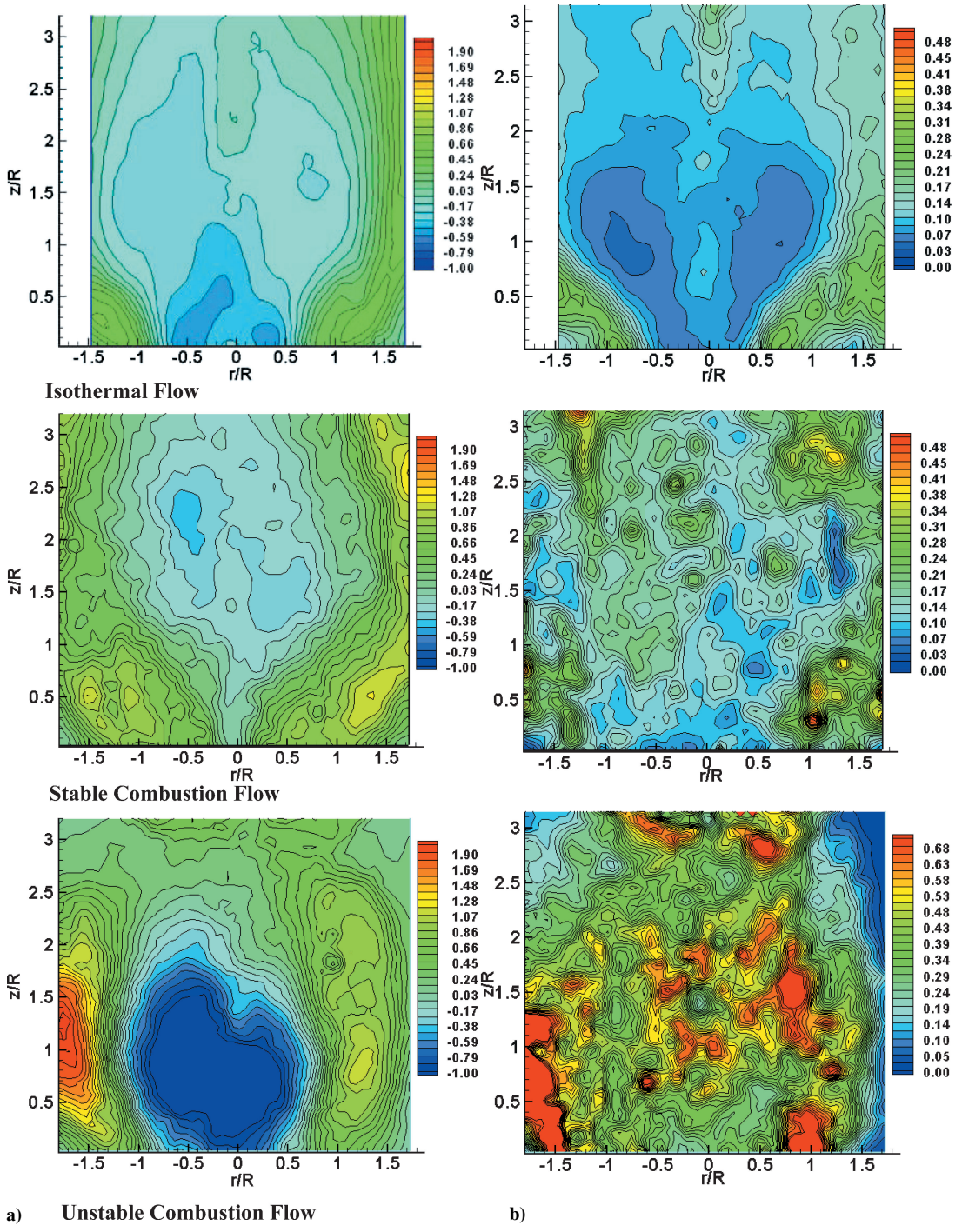

Fig. 5 Comparison of contours for isothermal, stable combustion and unstable combustion flows; $m_a = 0.032$ kg/s, $L_{mt} = 0$, and $C_R = 1$: a) V_z/V_0 and b) k/V_0^2.

reduced in size from a $3R$ wide and $3.5R$ long sphere for the isothermal case to a compact region with $2R$ width and $2.5R$ length and a significantly increased level of reversed axial velocity. In addition, the unstable combustion also caused asymmetric distribution of V_z at the left and right sides of the flow surrounding the CRZ (Fig. 5a, unstable combustion flow). Combustion dramatically affects the distribution of k/V_0^2, breaking the clearly defined low- and high-turbulence velocity regions of isothermal flow into dispersed form in the combustion cases (Fig. 5b).

To quantify the effect of combustion on the swirling flowfields, profiles of V_z/V_0, V_θ/V_0, V_r/V_0, and k/V_0^2 were extracted at $z/R = 0.2$ (Fig. 5) and are shown in Fig. 6. Compared with the isothermal case, the stable combustion forms much weaker recirculation flow at $z/R = 0.2$ due to the downstream shift of the CRZ (Fig. 6a), but with fairly similar V_θ/V_0 radial distribution (Fig. 6b). Unstable combustion causes stronger reversed flow (negative V_z) within $\pm 1R$ (Fig. 6a) and enhanced V_θ near $\pm 1.5R$ (Fig. 6b) compared to the isothermal and stable combustion cases. Combustion, either stable or unstable, greatly enhances the radial motion of the swirling flow to about twice that of the isothermal case (Fig. 6c at $r/R = \pm 1$). In terms of turbulent energy, in the vicinity of the nozzle exit, k/V_0^2 was similar for the stable combustion and isothermal cases (Fig. 6d); the unstable combustion, however, nearly doubled the magnitude of TKE relative to the isothermal and stable combustion cases in the range $\pm 1R$ (Fig. 6d). It was noticed that the flowfield of unstable combustion was asymmetric, although the boundary conditions for this case is symmetric as for the isothermal and the stable combustion case. Because unstable combustion in

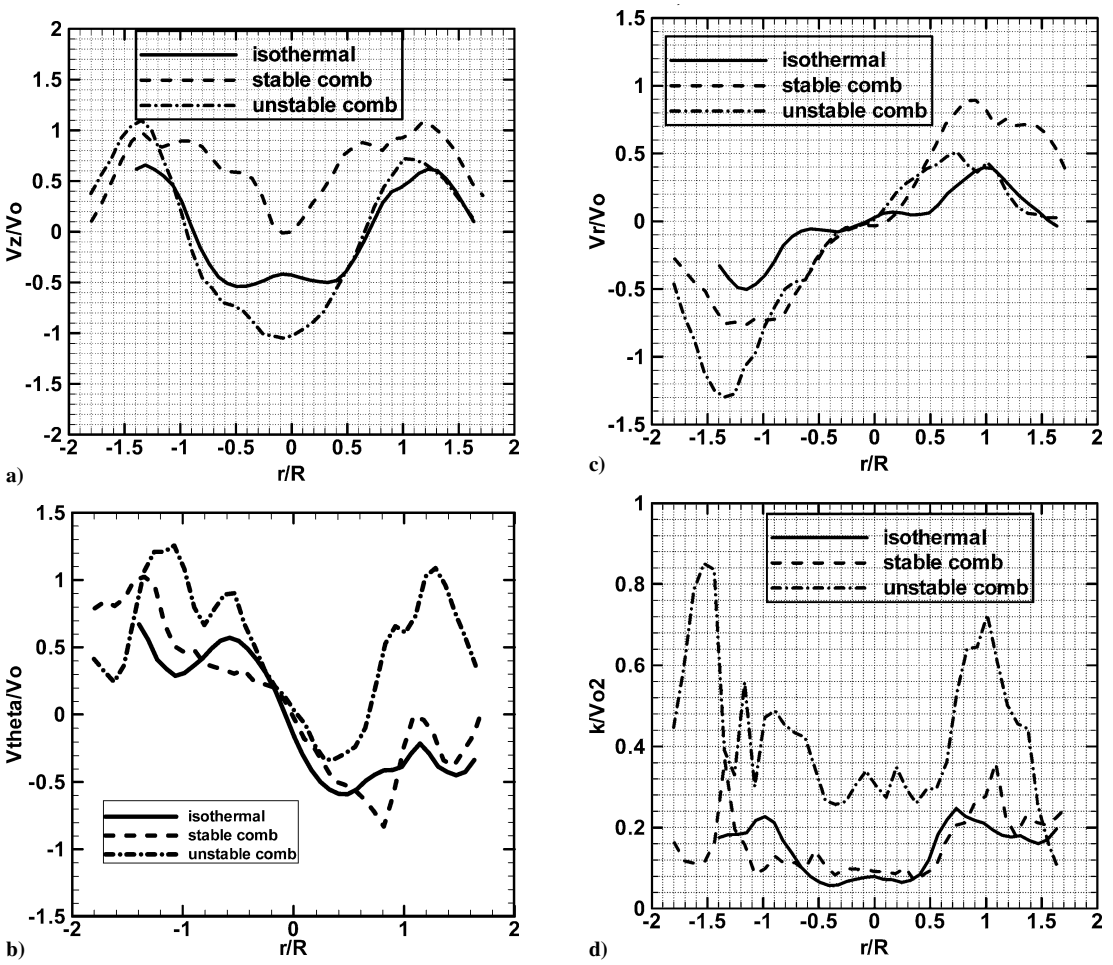

Fig. 6 Comparison of radial profiles at $z/R = 0.2$ for isothermal, stable, and unstable combustion cases; $T_3 = 230°C$, $m_a = 0.032$ kg/s, $L_{mt} = 0$, and $C_R = 1$: a) V_z/V_0, b) V_θ/V_0, c) V_r/V_0, and d) k/V_0^2.

the current combustor is closely related to unsteady heat release and pressure oscillations that may be manifested in time and space, it is suggested that the asymmetry of the velocity field could be caused by the changes in the combustion and temperature fields.

Spectra of velocity in the swirling flow. Information on the spectra of velocity fluctuations in turbulent swirling flows is important for properly modeling them. Constant temperature anemometer was used to measure the spectra of the confined turbulent swirling flow in the circular combustion chamber. The frequency was normalized by the TARS exit diameter D according to the following equation:

$$Sr = fV_0/D \tag{3}$$

where f is the frequency in hertz.

For the spectral measurements, the single straight wire was oriented perpendicular to V_z and V_θ velocity components and parallel to the V_r component such that the spectra represented fluctuations of both V_z and V_θ. Figure 7 shows the power spectra of V_z and V_θ at three axial locations, $z/R = 0$, 5, and 10 along the shear layer, at a constant radial distance of $r/R = 0.4$. For reference, the Kolmogorov $K^{-5/3}$ law is included. The high-frequency broadband peak at a frequency of $Sr = 3.3$, which is present in the initial jet shear layer, disappears immediately downstream. Next to the vortex breakdown region, at $z/R = 5$, the spectra has two peaks, $Sr = 0.16$ and 0.35. The second peak falls within the range of the jet-preferred mode, $Sr = 0.24$–0.64, as described by Schadow and Gutmark for flow in dump combustors.[13] This frequency may also be related to the flow dynamics of the precessing vortex core (PVC) associated with vortex breakdown, as suggested by Chao et al.[14] in the study of spectral characteristics of swirling flowfields. The lowest frequency,

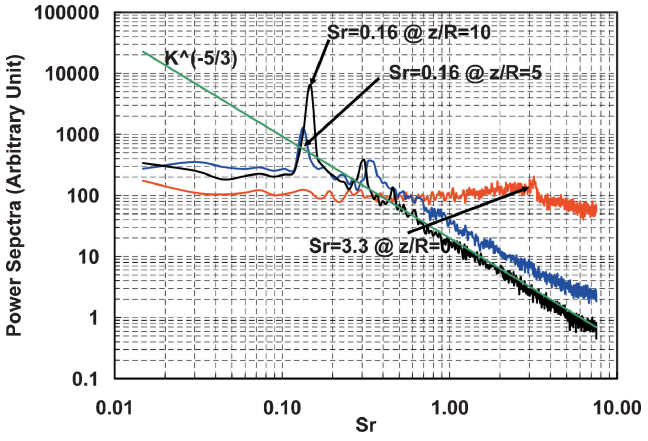

Fig. 7 Spectra of velocity (combined V_z and V_0 componants) at three locations of $r/R = 0.4$ inside swirling flow; $m_a = 0.032$ kg/s, $T_3 = 23°C$, $L_{mt} = 0$, and $C_R = 1$.

$Sr = 0.16$, dominated most of the swirling flow except in the proximity of the TARS exit. The amplitude of this low-frequency mode is amplified in the downstream direction. At $z/R = 10$, the flow is dominated by this low frequency, as is evidenced by the narrowband peak. Similar observations were made in the study of Chao et al.,[14] who found a dominant low frequency in the downstream of swirling flow and classified it to be "most amplified downstream azimuthal instability" and to be a strong function of the inlet Reynolds number and a weak function of swirl strength. Note that beyond $Sr = 0.5$ the

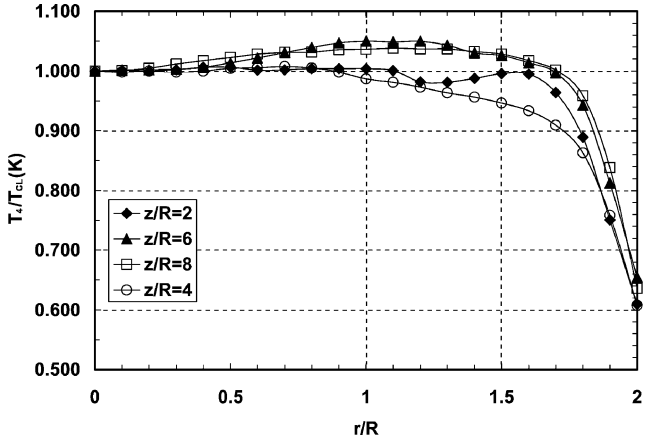

Fig. 8 Radial profiles of T_4/T_{CL} at different axial locations: gaseous propane, $\Phi = 0.57$, $m_a = 0.022$ g/s, $T_3 = 230°$C, $L_{mt} = 0$, and $C_R = 1$, octagonal combustor.

spectra at $z/R = 5$ and 10 are following the $K^{-5/3}$ slope, indicative of a fully developed turbulence.

2. Temperature Distribution

The radial distribution of the reacting flow temperature T_4 was measured using a fine type-B thermocouple at four axial locations, $z/R = 2$, 4, 6, and 8. The symmetry of the radial temperature profile {defined as $(T_1 - T_2)/[(T_1 + T_2)/2]$, where T_1 and T_2 are temperatures at two radially equidistant locations} was in the range of 0.3–1%. Therefore, only one-half of the temperature field is shown. The combustion gas temperature was normalized with the temperature at the centerline, T_{CL}. Figure 8 shows the radial temperature profiles for propane at an equivalence ratio $\Phi = 0.57$ and $T_3 = 230°$C. The overall temperature distribution is quite uniform in the main combustion region of $r/R = 0$–1.5 over an axial extent of $z/R = 2$–8. The temperature drops rapidly near the wall. Because the fuel spreads outward with the conical swirling air jet, the flame has also a conical shape as indicated by the temperature distribution.

3. OH Chemiluminescence Image*

It is commonly accepted that CH* and OH* chemiluminescence represents reaction or heat release rate if the integrated chemiluminescence is linearly related to fuel consumption and the electronically excited radicals are confined to a relatively thin region in the vicinity of the primary flame surface.[15] The primary source of OH* ($A^2\Delta$) is believed to be produced by oxidation of CH with transition around 308 nm. For overall flame structure characterization, the chemiluminescence image was taken with 10-ms exposure time. A bandpass filter centered at 308 nm was used to cut off interference from other radical emissions.

Figure 9 is the OH* image at $\Phi = 0.57$ and $T_3 = 230°$C for the baseline case. The color bar is the pixel value normalized by the background level. The flame was centered along the four airstreams that emanated from the swirler through the four vanes. Because the chemiluminescence is a line-of-sight integration, the intense flame located near the center is actually an overlap of the two front and aft flame sections. LDV measurements and three-dimensional RANS simulations showed that the flow in the cross-sectional plane is azimuthally asymmetric.[16] Air flowing through the vanes of the intermediate and outer swirlers has higher velocity and forms high-velocity regimes at the TARS exit plane. The number of high velocity airstreams matched the four vanes in the intermediate swirler. In a computational effort, it is necessary to include the mixer–swirler in the computational domain to capture the azimuthal asymmetry of the reacting swirling flow.

4. Emission Characteristics

Formation of emissions is a result of a combined effect of the swirling flowfield, the fuel distribution, the reaction characteristics, and the temperature distribution. Figure 10 shows the NO_x emissions

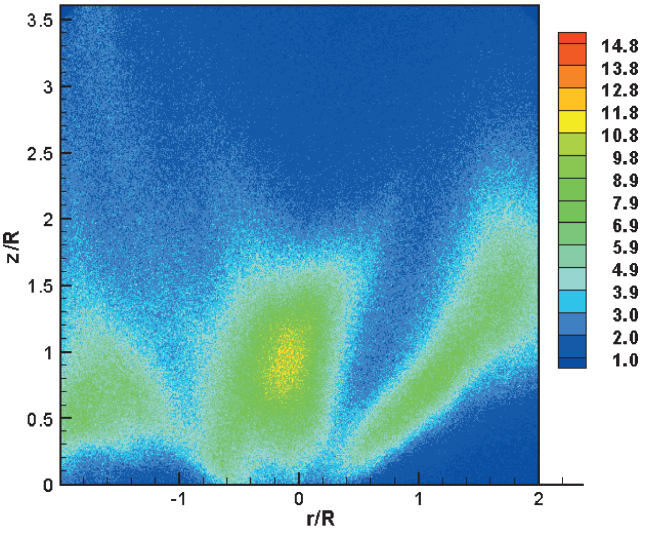

Fig. 9 OH* chemiluminescence image for baseline case: $\Phi = 0.57$, $T_3 = 230°$C, $m_a = 0.032$ kg/s, $L_{mt} = 0$, and $C_R = 1$.

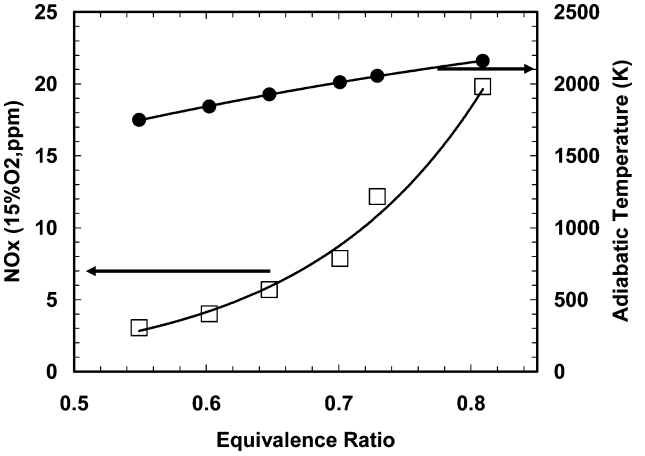

Fig. 10 Dependence of NO_x emissions and adiabatic temperature on fuel equivalance ratio: $m_a = 0.032$ kg/s, $T_3 = 230°$C, $L_{mt} = 0$, and $C_R = 1$, propane.

and calculated adiabatic equilibrium temperature at $T_3 = 230°$C. The NO_x is corrected to 15% O_2 value according to

$$(NO_x)_{15\%O2} = (NO_x)_{measured} \times 5.9/(20.9 - O_{2,measured}) \quad (4)$$

The adiabatic equilibrium temperature was calculated using the NASA CEA code. Formation of NO_x increases with the fuel equivalence ratio and the flame temperature. The baseline multiswirler design of this LDI combustion system has low NO_x emissions in a range of 4–18 ppm for $\Phi = 0.55$–0.81.

B. Effect of Inlet Boundary Conditions

The swirling flow is very sensitive to inlet boundary conditions as are combustion properties, including dynamics and emissions, which are closely related to the flowfield characteristics. As stated in the experimental setup section, a short mixing tube can be inserted between the TARS exit and the combustion chamber to convert the LDI arrangement to a premixed combustion configuration. This mixing tube not only provides additional volume for premixing fuel and air but also has significant impact on the swirling flowfield and the combustion process. The length of this mixing tube, L_{mt}, is an important inlet boundary condition for properly simulating complex nonreacting or reacting swirling flows. This section will emphasize the effect of the mixing tube length on the velocity profiles, velocity spectra, temperature distribution, and emissions.

Figure 11 shows the comparison of profiles of V_z/V_0 and V_θ/V_0 at $z/R=0.4$ for $L_{mt}=0$, 0.3, 0.55, and 0.8. When L_{mt} increases, the upstream stagnation point of the vortex breakdown region moves upstream into the mixing tube. The mixing tube increases V_z and V_θ velocity components of the downstream swirling jet surrounding the CRZ (Figs. 11a and 11b) and enhances the magnitude of the reversed flow (Fig. 11a). Close to the combustor inlet, the mixing tube formed a larger vortex core region extending to $r/R=\pm1$ (Fig. 11b) compared to the case without the mixing tube, where it extends only to $r/R=\pm0.5$. The three-dimensional vector field plot (Fig. 12) shows a pair of large vortical structures, which did not exist for $L_{mt}=0$, that were nested along the rolling flow structure for $L_{mt}=0.55$. These large vortices were also observed for $L_{mt}=0.3$ and 0.8, and their location moved upstream with increased L_{mt} (Ref. 17). Because the PVC structure is less likely to be damped in premixed combustion,[18] these vortices can potentially be responsible for the excitation of combustion dynamics.

The velocity spectra of $L_{mt}=0.55$ (Fig. 13) shows three frequency regimes along the swirling flow shear layer. The high frequency ($Sr=0.67$) is located in the initial shear layer of the swirling jet ($z/R=0$) and the low frequency ($Sr=0.15$) is located farther downstream ($z/R=10$). Compared to the high frequency $Sr=3.3$ of $L_{mt}=0$, the high frequency of $L_{mt}=0.55$ is much lower. Because with a longer mixing tube the combustor acquires features of dump combustor geometry, the high frequency may be related to the most amplified initial shear layer frequency as found in dump combustors. The intermediate frequency ($Sr=0.37$), which is the secondary peak of $L_{mt}=0$ at $z/R=5$, becomes the dominant frequency along the vortex breakdown region, suggesting that the mixing tube promotes stronger dynamics of the vortical structures observed in the three-dimemsional vector plot (Fig. 12). For $L_{mt}=0.55$, the $-\frac{5}{3}$ slope appears in the spectra between $Sr=0.5$–2, and the spectra of higher frequency has an even higher slope, indicating reaching a fully developed turbulence and stronger dissipation at high frequencies compared to the $L_{mt}=0$ case in Fig. 7.

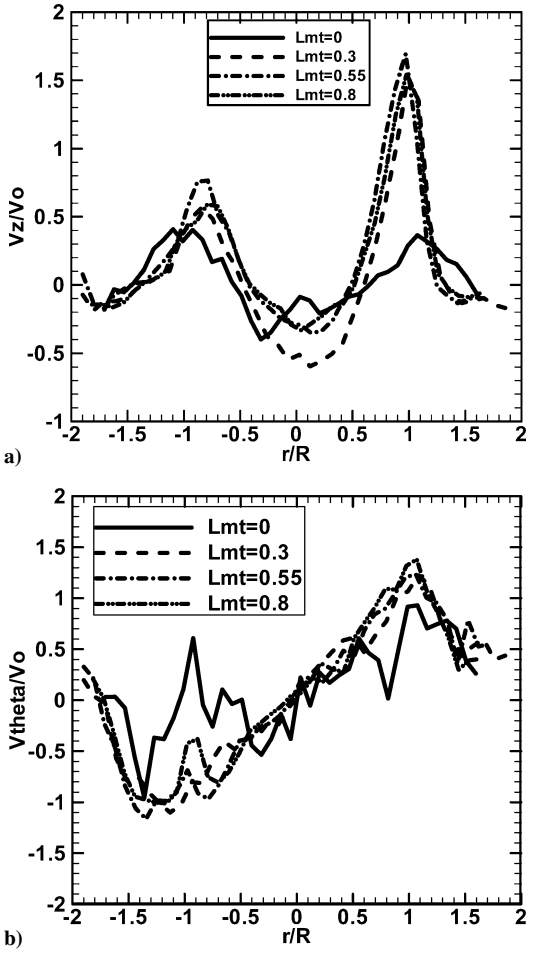

Fig. 11 Comparison of profiles at $z/R=0.4$ for $L_{mt}=0$, 0.3, 0.55, and 0.8, $m_a=0.032$ kg/s, $T_3=25°$C, and $C_R=4$: a) V_z/V_0 and b) V_θ/V_0.

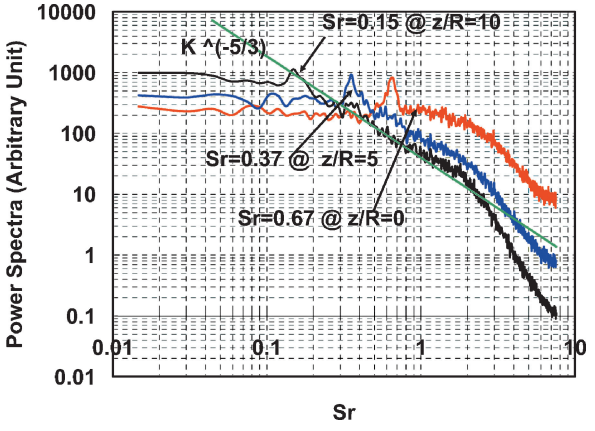

Fig. 13 Spectra of velocity on three locations of $r/R=0.4$, $z/R=0$, 5, and 10, inside the swirling flow; $m_a=0.032$ kg/s, $T_3=23°$C, and $L_{mt}=0.55$.

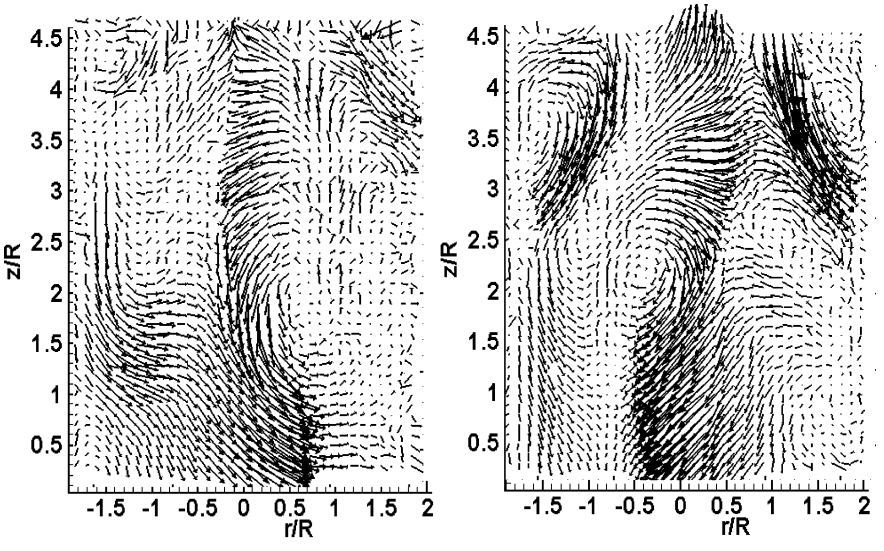

Fig. 12 Three-dimensional vector field for $L_{mt}=0$ and 0.55; $m_a=0.032$ kg/s, $T_3=23°$C, and $C_R=4$.

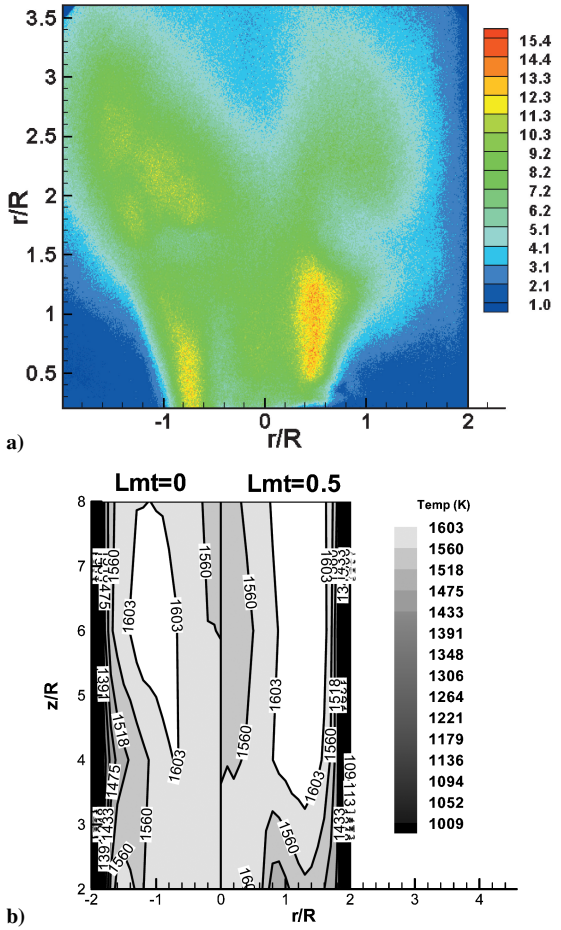

Fig. 14 Effects of mixing tube length on heat release and temperature: a) OH* chemiluminescence image for $L_{mt} = 0.5$, $\Phi = 0.57$, $T_3 = 230°C$, $m_a = 0.032$ kg/s, and $C_R = 1$ and b) comparison of temperature distribution for $L_{mt} = 0$ and 0.5, $\Phi = 0.5$, $T_3 = 230°C$, $m_a = 0.026$ kg/s, and $C_R = 1$.

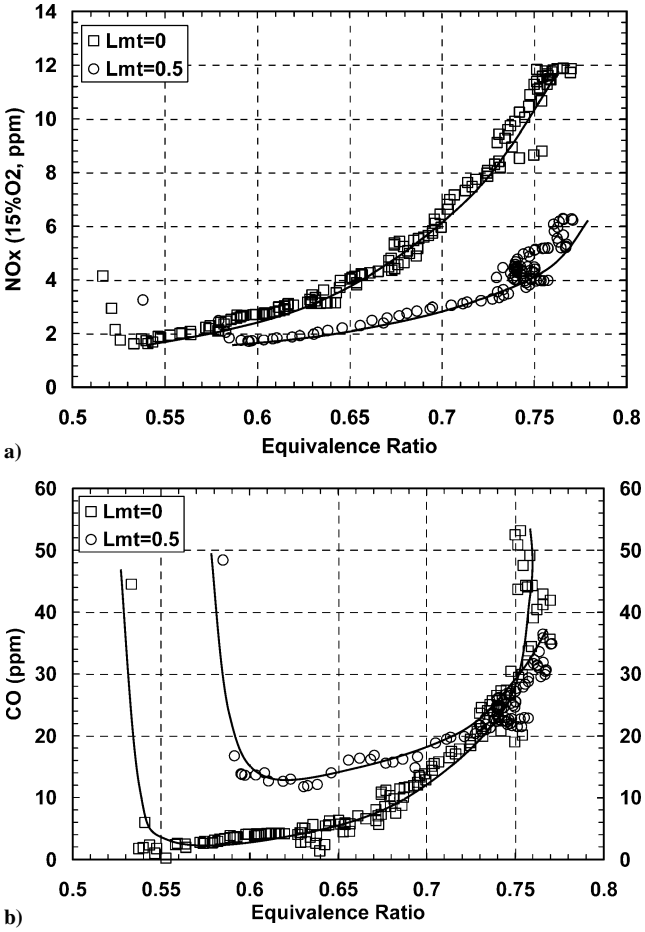

Fig. 15 Comparison of NO_x and CO for $L_{mt} = 0$ and 0.5; $C_R = 1$, $T_3 = 230°C$, and $m_a = 0.032$ kg/s.

Figure 14 shows the flame OH* chemiluminescence for $L_{mt} = 0.5$ and a comparison between the temperature distribution of $L_{mt} = 0$ and 0.5. Compared with the OH* image of $L_{mt} = 0$ (Fig. 9), the insertion of the mixing tube stretched the flame, pulled it into the mixing tube, and reduced the flame lateral expansion. The temperature field showed very similar peak temperatures of >1600 K for both $L_{mt} = 0$ and 0.5; however, the region of high temperature is larger and is shifted toward the walls with the mixing tube. The NO_x emissions (Fig. 15a) were halved by the mixing tube for $\Phi = 0.6$–0.76. The shorter residence time caused by the increased jet velocity of $L_{mt} = 0.5$ is the key for NO_x reduction. Conversely, residence time affects the oxidation of CO, producing more CO for $L_{mt} = 0.5$ than $L_{mt} = 0$ (Fig. 15b). The mixing tube has an adverse effect on the flame stability, shifting the equivalence ratio of LBO, Φ_{LBO}, from $\Phi_{LBO} = 0.52$ for $L_{mt} = 0$ to $\Phi_{LBO} = 0.6$ for $L_{mt} = 0.5$. This is a result of the flame with the configuration that includes the mixing tube being stabilized primarily by the weakened CRZ stagnation region, whereas with no mixing tube the flame is also stabilized by the dump plane recirculation zone.

C. Effect of Outlet Boundary Conditions

Experimental studies[14,19] regarding the effect of the exhaust area contraction ratio C_R on the shape of the CRZ have shown that the downstream boundary conditions at the exhaust nozzle can affect the upstream flowfield if the flow remains in a subcritical state after vortex breakdown. However, these studies were limited to nonreacting flows. To emphasize the importance of exit boundary conditions of the combustor, which are sometimes neglected in computational studies, this section addresses the significant influence of downstream exit conditions on nonreacting and reacting flows.

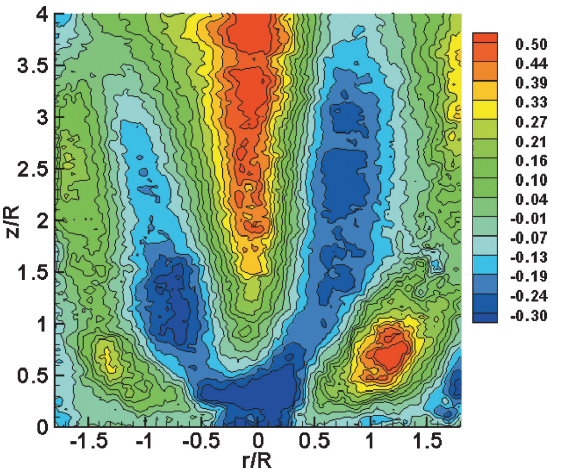

Fig. 16 Contours of V_z/V_0 at $C_R = 4$; $m_a = 0.032$ kg/s, $L_{mt} = 0$, and $T_3 = 23°C$.

The contours of V_z/V_0 component for $C_R = 4$ (Fig. 16) illustrates the effect of the downstream contraction on CRZ: The shape of CRZ (blue color in the contour plot) changed from a spherical shape (Fig. 3 V_z/V_0) of $C_R = 1$ to a conical V shape for large contraction ratio of $C_R = 4$. The larger contraction ratio caused the recirculation zone to collapse near the centerline, forcing the reversed flow to recover back to the downstream direction and moved the location of downstream stagnation point from $z/R = 4$ for $C_R = 1$ to $z/R = 0.5$ for $C_R = 4$. Profiles of V_z/V_0 at $z/R = 2$ for $C_R = 1.14$–4 (Fig. 17a) clearly show the recovery process of reversed flow at the central flow region (negative V_z) within $r/R = \pm 1$. Outside this region, profiles

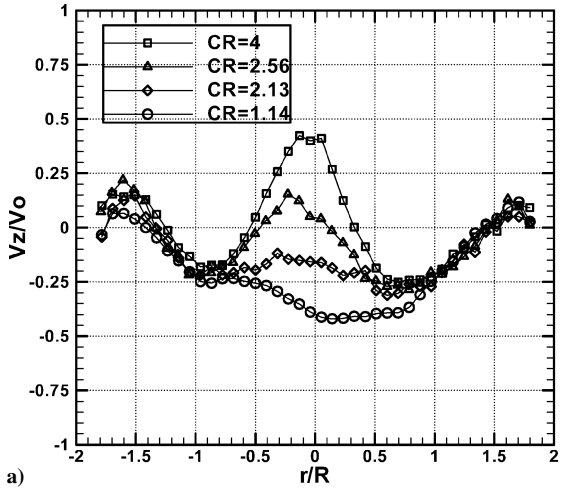

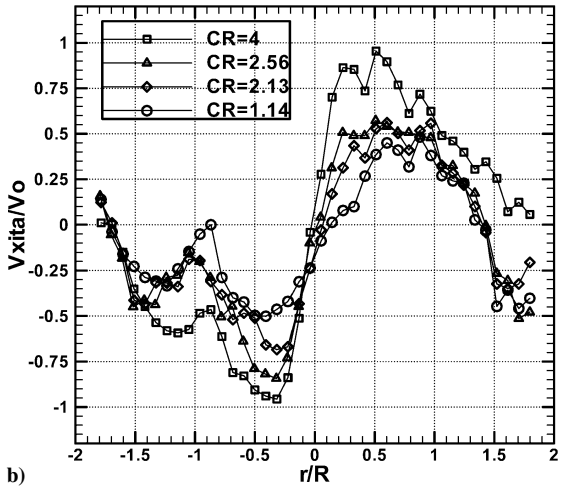

Fig. 17 Comparison of velocity profiles for $C_R = 1.14$, 2.13, 2.56, and 4 at $z/R = 2$; $m_a = 0.032$ kg/s, $L_{mt} = 0$, and $T_3 = 23°C$: a) V_z/V_0 and b) V_θ/V_0.

V_z/V_0 remain unchanged for all C_R. The V_θ component (Fig. 17b) shows that the split of the recirculation zone in the central region for large nozzle constriction results in a 50% increase in the magnitude of this component as C_R changes from 1.14 to 4. This is accompanied by an increase in the radial slope of the V_0 velocity in the vortex core region. Large contraction of the combustor exit introduces a transformation in the CRZ shape and a stronger rotation of the vortex core.

Velocity spectra provided additional information on the effect of the downstream contraction. Figure 18 presents the velocity spectra of V_z and V_θ components for $C_R = 4$ at a fixed radial location $r/R = 0.4$, at three axial locations along the shear layer of the swirling flow, $z/R = 0$, 5, and 10. A comparison of these spectra with those corresponding to the baseline case shows the following results:

1) High-frequency velocity fluctuations, $Sr = 3.2$, are still dominant close to the TARS exit ($z/R = 0$). The Strouhal number of the high frequency remains nearly the same for $C_R = 1$ and 4 and is not affected by the exhaust nozzle contraction ratio.

2) The low frequency of $Sr = 0.15$ at $z/R = 10$ is less dominant for $C_R = 4$ than for $C_R = 1$, indicating the dampening effect of the contraction on this low frequency in the downstream flow region.

3) The middle range frequency of $Sr = 0.37$ is amplified for large contraction. This frequency is located at the inner shear layer formed between the recovered downstream flow and the reversed flow at the vicinity of the burner axis. Therefore, it is proposed that the downstream contraction augments the precessing vortices in the central vortex breakdown region. For $z/R > 5$, the turbulence spectra reaches a fully developed state as indicated by the $-\frac{5}{3}$ slope.

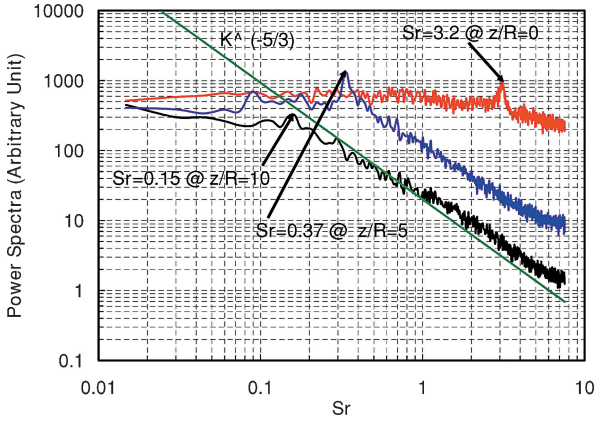

Fig. 18 Spectra of velocity of V and W componants at locations $r/R = 0.4$, $z/R = 0$, 5, and 10 for $C_R = 4$; $m_a = 0.032$ kg/s, $L_{mt} = 0$, and $T_3 = 23°C$.

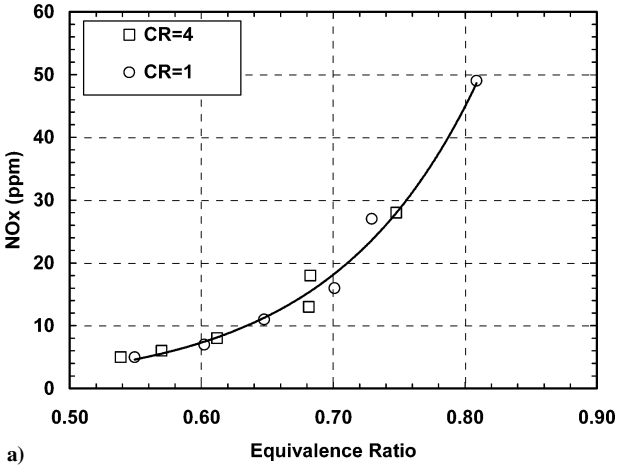

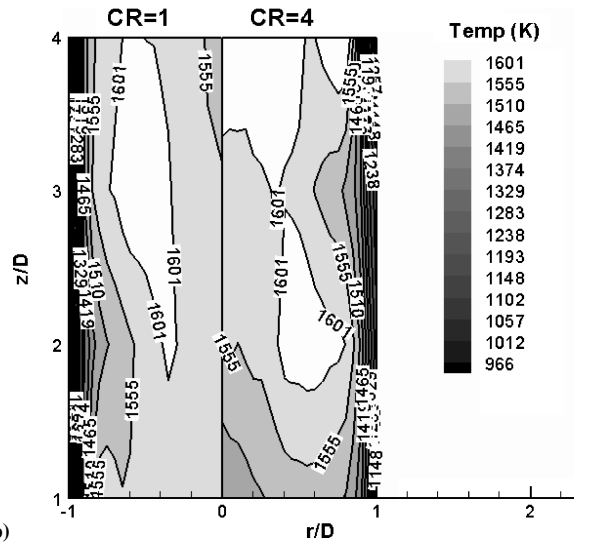

Fig. 19 Comparisons with gaseous fuel, $T_3 = 230°C$, and $m_a = 0.026$ kg/s: a) NO_x emissions and b) temperature distribution at $\Phi = 0.5$ between $C_R = 1$ and 4.

The comparison of NO_x emissions and temperature distribution for $C_R = 1$ and $C_R = 4$ is shown in Fig. 19. In the present case, for gaseous fuel with high inlet air temperature, NO_x increased exponentially with the lean equivalence ratio, that is, with flame temperature, following the same trend line for both contraction ratios over the range of $\Phi = 0.54$–0.75. OH^* chemiluminescence showed that the flame structure of the two cases was nearly identical.[20] The temperature fields of the two contraction ratios showed nearly uniform

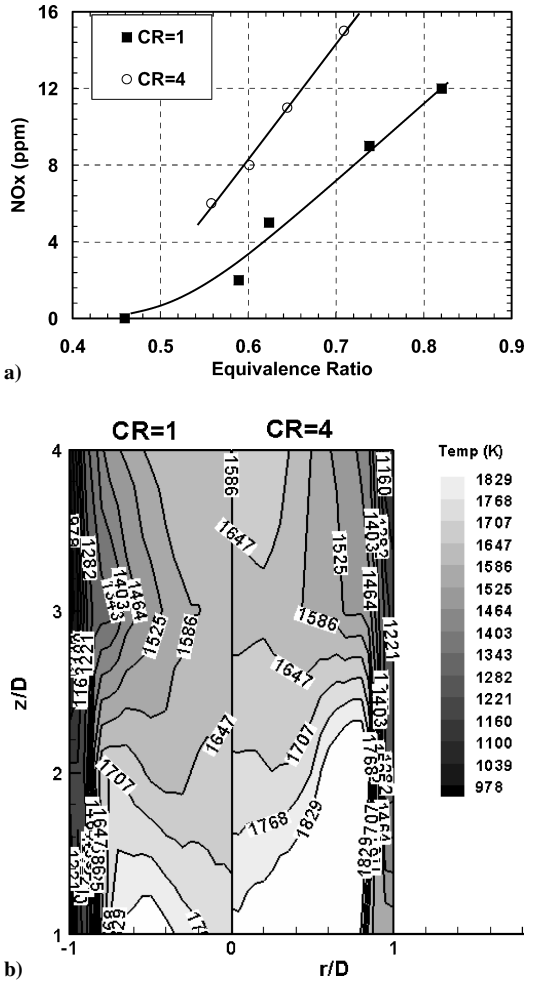

Fig. 20 Comparisons with ethanol, $T_3 = 230°C$, and $m_a = 0.032$ kg/s: a) NO_x emissions and b) temperature distribution $\Phi = 0.5$ between $C_R = 1$ and 4.

distributions with temperatures ranging from 1550 to 1600 K. These results suggest that the flame structure and the emissions characteristics were not sensitive to the downstream contraction ratios for gaseous fuel with the present combustor geometry. This observation confirms the hypothesis suggested by Escudier and Keller[19] that the subcritical state observed in cold vortex breakdown tests may disappear in combustion. The fast expansion that increases the axial velocity and the stronger viscous effects resulting from the elevated temperature field promote transition from subcritical to supercritical state upstream of the combustor exit.

The results are different for liquid spray combustion for different contraction ratios. Figure 20 shows the NO_x emissions and temperature distribution for $C_R = 1$ and 4 with ethanol fuel. NO_x level for $C_R = 4$ was nearly twice as high as that of $C_R = 1$. Regarding the temperature contours, the large contraction increased the peak temperature from 1707 K for $C_R = 1$ to 1829 K for $C_R = 4$, and the high-temperature region was significantly enlarged. The temperature field was also affected by the V-shaped CRZ induced by the large contraction. In this case, properly modeling the downstream contraction is vital for an accurate computational simulation.

IV. Conclusions

The present study investigated the detailed three-dimensional swirling flow velocity statistics, temperature distribution, OH^* chemiluminescence, and NO_x and CO emissions characteristics of a multiswirl low-NO_x combustor. This experimental study emphasized the significant impact of inlet and outlet boundary conditions on the nonreacting and reacting flows.

Increased air inlet temperature enhanced the magnitude of reversed flow in the central region and increased the tangential velocity in the swirling jets and the energy of the turbulent velocity fluctuations. These effects can contribute to the typical NO_x increase with higher inlet air temperatures and can be explained in terms of enhanced reaction and heat release rate and increased residence time.

An addition of a mixing tube in the combustor inlet did not only serve as an additional mixing volume for fuel and air, but also led to aerodynamic changes of the swirling flowfield. It had an effect on the magnitude of the axial and tangential mean velocity components and on the formation of large vortical structures in the CRZ. NO_x emissions were substantially reduced with the mixing tube due to these effects, but increased CO production and reduced flame stability were observed.

The contraction ratio of the combustor exhaust nozzle transformed the shape of the recirculation zone from a spherical shape to a conical recirculation zone and greatly increased the tangential velocity inside the vortex core. Although NO_x formation for different contraction ratios were comparable with gaseous fuel, the dramatic influence on the temperature distribution and NO_x emissions of liquid spray combustion emphasizes the importance of downstream boundary conditions.

References

[1]Gupta, A. K., "Gas Turbine Combustion: Prospects and Challenges," *Energy Conversation Management*, Vol. 38, No. 10–13, 1997, pp. 1311–1318.

[2]Doebbling, K., Knopfl, H. P., Polifke, W., Winkler, D., Steinback, C., and Sattelmayer, T., "Low-NOx Premixed Combustion of Mbtu Fuels Using the ABB Double Cone Burner (EV Burner)," *Journal of Engineering for Gas Turbines and Power*, Vol. 118, Jan. 1996, pp. 46–53.

[3]Snyder, T. S., Rosfjord, T. J., McVey, J. B., Hu, A. S., and Schlein, B. C., "Emission and Performance of a Lean-Premixed Combustion Gas Fuel Injection System for Aeroderative Gas Turbine Engines," *Journal of Engineering for Gas Turbines and Power*, Vol. 118, Jan. 1996, pp. 38–45.

[4]Docquier, N., and Candel, S., "Combustion Control and Sensors: A Review," *Progress in Energy and Combustion Science*, Vol. 28, No. 2, 2002, pp. 107–150.

[5]Sanborn, J. M., Mongia, H. C., and Kidwell, J. R., "Design of a Low Emissions Combustor for an Automotive Gas Turbines," AIAA Paper 83-0338, Jan. 1983.

[6]Gupta, A. K., Ong, L. H., and Marchionna, N., "NOx Reduction and Combustion Phenomena in the Multi-Annular Gas Turbine Swirl Burner," AIAA Paper 87-2036, Jan. 1987.

[7]Hussain, U. S., Andrews, G. E., Cheung, W. G., and Shahabadi, A. R., "Low NO_x Primary Zones Using Jet Mixing Shear Layer Combustion," American Society of Mechanical Engineers, ASME Paper 88-GT-308, 1988.

[8]Terasaki, T., and Hayashi, S., "The Effects of Fuel-Air Mixing on NO_x Formation in Non-Premixed Swirl Burners," *Proceeding of the Twenty-Sixth Symposium (International) on Combustion*, Combustion Inst., Naples, Italy, 1996, pp. 2733–2739.

[9]Grinstein, F. F., Young, T. R., Gutmark, E. J., Li, G., Hsiao, G., and Mongia, H., "Flow Dynamics in a Swirl Combustor," *Journal of Turbulence*, Vol. 3, July 2002.

[10]Wang, S., and Young, V., "Modeling of Gas Turbine Swirl Cup Dynamics, Part 5: Large Eddy Simulations of Cold Flow," AIAA Paper 2003-6105, Jan. 2003.

[11]Cannon, S. M., and Smith, C. E., "LES Predictions of Combustor Emissions in an Aero Gas Turbine Engine," AIAA Paper 2003-4521, Jan. 2003.

[12]Shaddix, C. R., "Correcting Thermocouple Measurements for Radiation Loss: A Critical Review," *33rd National Heat Transfer Conference*, American Society of Mechanical Engineers, Paper HTD99-282, 1999.

[13]Schadow, K., and Gutmark, E., "Combustion Instability Related to Vortex Shedding in Dump Combustors and Their Passive Control," *Progress in Energy and Combustion Sciences*, Vol. 18, No. 2, 1992, pp. 117–132.

[14]Chao, Y. C., Leu, J. H., and Hung, Y. F., "Downstream Boundary Effects on the Spectral Characteristics of a Swirling Flow Field," *Experiments in Fluids*, Vol. 10, 1991, pp. 341–348.

[15]Najm, H. N., Paul, P. H., Mueller C. J., and Wyckoff, P. S., "On the Adequacy of Certain Experimental Observables as Measurements of

Flame Burning Rate," *Combustion and Flame*, Vol. 113, No. 3, 1998, pp. 312–332.

[16]Li, G., and Gutmark, E. J., "Experimental and Numerical Studies of the Velocity Field of a Triple Annular Swirler," *Proceeding of 2002 International Gas Turbine Institute*, American Society of Mechanical Engineers, GT-2002-30069, 2002.

[17]Li, G., and Gutmark, E. J., "Flowfield Measurement of a Triple Swirler Spray Combustor," AIAA Paper 2002-4010, June 2002.

[18]Syred, N., and Beer, J. M., "Combustion in Swirling Flow: A Review," *Combustion and Flame*, Vol. 23, 1974, pp. 143–201.

[19]Escudier, M. P., and Keller, J. J., "Recirculation in Swirling Flow: A Manifestation of Vortex Breakdown," *AIAA Journal*, Vol. 23, No. 1, 1985, pp. 111–116.

[20]Li, G., and Gutmark, E., "Effects of Exhaust Nozzle Geometry on Combustor Flow Field and Combustion Characteristics," *Proceeding of the Thirtieth Symposium (International) on Combustion*, Combustion Inst., 2004.

F. Grinstein
Guest Editor